Extended B-Site Vacancy Content Range and Cation Ordering in Twinned Hexagonal Perovskites Ba 8 Cr 4– x Ta 4+0.6 x O 24

Weiwei Cao, Xiaoyan Yang, Cécile Genevois, Mathieu Allix, Xiaojun Kuang

Extended B-Site Vacancy Content Range and Cation Ordering in Twinned Hexagonal Perovskites $Ba_8Cr_{4-x}Ta_{4+0.6x}O_{24}$

Weiwei Cao [†, ‡, #], *Xiaoyan Yang* [†,#], *Cécile Genevois* [‡], *Mathieu Allix* [*,‡], *Xiaojun Kuang* [*, †, ⊥]

[†] MOE Key Laboratory of New Processing Technology for Nonferrous Metal and Materials, Guangxi Key Laboratory of Optical and Electronic Materials and Devices, College of Materials Science and Engineering, Guilin University of Technology, Guilin 541004, P. R. China

[‡] CNRS, CEMHTI UPR3079, Univ. Orléans, F-45071 Orléans, France

[⊥] College of Chemistry and Bioengineering, Guilin University of Technology, Guilin 541004, P. R. China

[#] These two authors equally contribute to this work.

* E-mail: mathieu.allix@cnrs-orleans.fr (M.A.); kuangxj@glut.edu.cn (X.K.)

◘ ABSTRACT

A new 8-layer twinned hexagonal solid solution $Ba_8Cr_{4-x}Ta_{4+0.6x}O_{24}$ (x = 0.0-3.0) was isolated through the aliovalent substitution of Ta^{5+} for Cr^{3+} in Ba_2CrTaO_6, showing the widest B-site vacancy content range among the 8-layer twinned hexagonal perovskites. $Ba_8Cr_{4-x}Ta_{4+0.6x}O_{24}$ forms a simple 8-layer hexagonal perovskite structure within $0.0 \leq x < 2.4$, and a tripled 8-layer hexagonal perovskite superstructure within $2.4 \leq x \leq 3.0$. The later shows expanded a and b axes by $\sqrt{3}$ times compared to the simple 8-layer hexagonal perovskite structure owing to the partial face-sharing octahedral (FSO) B cation ordering along the *ab* plane. The B-cation and vacancy distributions in the tripled superstructure were characterized by neutron and X-ray powder diffraction and further confirmed by scanning transmission electron microscopy-high angle annular dark field imaging and intensity profile analysis. The formation of 8-layer twinned hexagonal perovskites $Ba_8Cr_{4-x}Ta_{4+0.6x}O_{24}$ in an extended solid solution range can be attributed to the presence of both covalent B-B and B-O-B bonding and B-site vacancies in the FSO sites. This work provides an effective way of combining covalent B-B and B-O-B bonding and vacancy creation as well as the cationic ordering in the FSO sites to reduce electrostatic repulsion which could further enable the stabilization of new hexagonal perovskite compounds.

◘ INTRODUCTION

Hexagonal perovskite oxides with mixed cubic (*c*) and hexagonal (*h*) stacking of AO_3 layers have received considerable interest owing to their structural diversity and technologically important physical properties such as high dielectric constant[1-4], ionic mobility[5, 6], photocatalytic activity,[7-9] etc. The hexagonal stacking introduces face sharing octahedral (FSO) units with shorter B-B contacts compared with those in corner-sharing octahedral (CSO) block. This may result in significant electrostatic repulsion between the FSO B cations, which could destabilize the hexagonal perovskite structure. Therefore hexagonal perovskites usually form *B*-site deficient compositions with FSO B-site vacancies, favorable for reducing the FSO B-B electrostatic repulsion[7, 10]. B-site fully occupied hexagonal perovskites are less but often observed in transitional metal containing oxides since the semimetal B–B bonding form in the FSO sites to relieve the B–B electrostatic repulsion such as in manganates.[11]

Recently, the 8-layer *B*-site deficient twinned hexagonal tantalate perovskites $Ba_8MTa_6O_{24}$ (M = Zn, Ni, Co)[2, 12-14] have drawn much attention owing to their high quality factors, showing potential application as microwave dielectric resonators, on which there are great demand particularly for the development of new 5G mobile communication technology[15, 16]. This stimulated further synthesis of new analogues through changing the M^{2+} cations e.g. on $Ba_8CuTa_6O_{24}$[13] and $Ba_8MnTa_6O_{24}$[7] compositions or introducing trivalent cations, leading to the formation of $Ba_8Ga_{4-x}Ta_{4+0.6x}O_{24}$[17] compounds with variable B-site vacancy content covering from 10% to 16%, in contrast with the fixed vacancy content at 12.5% in $Ba_8MTa_6O_{24}$ and a narrow range of 12.5-14.5% vacancy content in $Ba_8Ti_{3-x}Ta_{4+0.8x}O_{24}$[18]. So far $Ba_8Ga_{4-x}Ta_{4+0.6x}O_{24}$ possesses the widest B-site vacancy content range, which is the only one example of 8-layer twinned hexagonal perovskite displaying B-site vacancy content below 12.5%.[17] However, the

8-layer twinned structure does not extend to the Ga-rich end member Ba_2GaTaO_6 presumably with pure Ga_2O_9 FSO dimer in $Ba_8Ga_{4-x}Ta_{4+0.6x}O_{24}$, revealing that FSO Ga-Ga dimer is an unstable configuration.

Ba_2CrTaO_6[19] has been known as a line phase for more than 25 years, and adopts an 8-layer twinned hexagonal structure with FSO and CSO B sites respectively fully occupied by Cr and Ta cations. In this B-site fully-occupied structure, chromium atoms in the FSO dimers form semimetal covalent Cr-Cr and 90° Cr-O-Cr bonding, which decreases the FSO B-B electrostatic repulsion. However, there was no attention on whether this structure is able to accommodate vacancies on the FSO B-sites. In this study, through aliovalent substitution of Ta^{5+} for Cr^{3+} in Ba_2CrTaO_6 an 8-layer twinned hexagonal solid solution $Ba_8Cr_{4-x}Ta_{4+0.6x}O_{24}$ (x = 0.0-3.0) was successfully isolated, showing the widest range of FSO B-site vacancy content among the 8-layer twinned hexagonal perovskites. The B-cation and vacancy distributions were characterized by neutron and X-ray powder diffraction and further confirmed by scanning transmission electron microscopy-high angle annular dark field imaging and intensity profile analysis.

◘ EXPERIMENTAL

Synthesis. Polycrystalline $Ba_8Cr_{4-x}Ta_{4+0.6x}O_{24}$ (x = 0.0-4.0) materials were synthesized by traditional high-temperature solid-state reaction method in N_2 inert atmosphere to avoid oxidation of Cr^{3+}. Starting materials of Ba_2CO_3 (99%, Aladdin), Cr_2O_3(99%, Aladdin) and Ta_2O_5 (99.99%, Aladdin) were weighed according to the correct stoichiometries and mixed with ethanol in an agate mortar for ~ 45 min to reach homogeneousness. The mixtures were pressed uniaxially into pellets, which were calcined at 750 °C for 1 h using heating and cooling rates of 5 °C/min, then were ball-milled for 9 h and repressed into pellets with a thickness ~ 7 mm in

height and ~ 10 mm in diameter by a cold-isostatic pressing facility under pressure 250 MPa for 20 min. The pellets were sintered at 1525 °C for 6 h to get dense ceramic for electrical characterizations and microwave dielectric performance measurements. The densities of the pellets were calculated using their weights and dimension sizes.

Characterization. Phase assemblage was investigated by X-ray powder diffraction (XRPD), which was performed using a Panalytical X'Pert PRO diffractometer running with Cu Kα radiation. High-quality XRPD data for Rietveld analysis were collected on a Bragg-Brentano D8 Advance Bruker laboratory diffractometer equipped with a LynxEye XE detector. Neutron powder diffraction (NPD) data were collected at the 3T2 station using a step size of 0.05° and wavelength of λ = 1.225 Å at the LLB laboratory (Saclay, France). The XRD and NPD data were analyzed by the Rietveld method[20], which was performed using TOPAS-Academic (V5) software[21]. Bond valance sums (BVS) were calculated by the method of Brown and Altermatt[22]. Selected area electron diffractions (SAED) were performed on a Philips CM20 transmission electron microscopy (TEM) operating at 200 kV. The fine sample powders were homogeneously dispersed in ethanol and deposited on a carbon-coated molybdenum grid before the TEM measurement. High resolution scanning transmission electron microscopy-high angle annular dark field (STEM-HAADF) imaging and X-ray energy dispersive spectroscopy (EDS) elemental mapping were performed at 200 kV using a JEOL-ARM200 Cold FEG microscope equipped with a double spherical aberration correctors and fitted with a JEOL SDD CENTURIO EDS system. The STEM-HAADF images and EDS maps were acquired with a 1 Å and 1.3 Å probe size respectively. The morphology examination for the ceramic samples were performed on ZEISS Gemini SEM 300 scanning electron microscope (SEM, Germany), equipped with

OXFORD EDS analyzer (ULTIM MAX 170, U.K.) and the elemental mapping analyses were also performed during the SEM experiments.

The oxidation state of Cr was measured by X-ray Photoelectron Spectroscopy (XPS) using a Thermo Fisher Scientific ESCALAB 250xi X-ray Photoelectron Spectrometer with a monochromatic Al Kα (1486.6 eV) X-ray beam. The binding energies are corrected based on the C 1*s* peak (284.6 eV). The peak deconvolutions were carried out using the XPSPEAK software based on a combination of Gaussian-Lorentzian peak function and Shirley background subtraction method.

Microwave dielectric properties were measured with Hakki-Coleman dielectric resonator method[23] with the TE_{011} mode using Agilent network analyzer N5230A. Temperature coefficients of resonance frequency τ_f were measured from RT up to 85 °C. AC impedance spectroscopy measurement was implemented by a Solartron 1260A impedance/gain-phase analyzer over the frequency range from 10^{-1} to 10^7 Hz on the pellets, which were painted with platinum paste on both front and back surfaces and heated at 700 °C for 30 min to remove organic component and form electrodes.

◘ RESULTS

$Ba_8Cr_{4-x}Ta_{4+0.6x}O_{24}$ solid solution. Figure 1a and Figure S1 show the XRPD data of $Ba_8Cr_{4-x}Ta_{4+0.6x}O_{24}$ (x = 0.0-4.0) fired at 1525 °C for 6 h, which indicate that compositions x = 0.0-3.0 form an 8-layer twinned hexagonal perovskite solid solution. Careful examination of XRPD data (Figure 1a) reveals that compositions within the $0.0 \leq x < 2.4$ range formed simple 8H phases; while the $2.4 \leq x \leq 3.0$ compositions form a tripled superstructure of the simple 8H phase, as indicated by the appearance of several extra weak reflections highlighted in the rectangles in

Figure 1a. The relatively weak but obvious peak of the x = 2.4 composition in 20.7- 22° 2Theta range witnesses the transition process from simple to tripled 8H phase. The tripled 8H phase has an enlarged *ab* plane, 3 times of that in the simple 8H phase, similar to $Ba_8Ga_{4-x}Ta_{4+0.6x}O_{24}$[17] and $Ba_8MTa_6O_{24}$ (M= Zn, Ni) cases.[2, 24] The compositions within $3.2 \leq x \leq 3.8$ form a mixture of tripled 8H phase and $Ba_5Ta_4O_{15}$ phase and the end-member composition (x = 4.0) forms a 5-layer shifted hexagonal perovskite phase, namely $Ba_5Ta_4O_{15}$ (Figure S1). The refined cell parameters of $Ba_8Cr_{4-x}Ta_{4+0.6x}O_{24}$ (Figure 1b) linearly increase with x within the $0.0 \leq x \leq 3.0$ region, obeying the Vegard's law[25] and consistent with the Ta^{5+} (0.64 Å) substitution for the smaller Cr^{3+} (0.615 Å).[26] Beyond point x = 3.0, the cell parameters remain almost constant, confirming the solid solution limit close to $x \leq 3.0$.

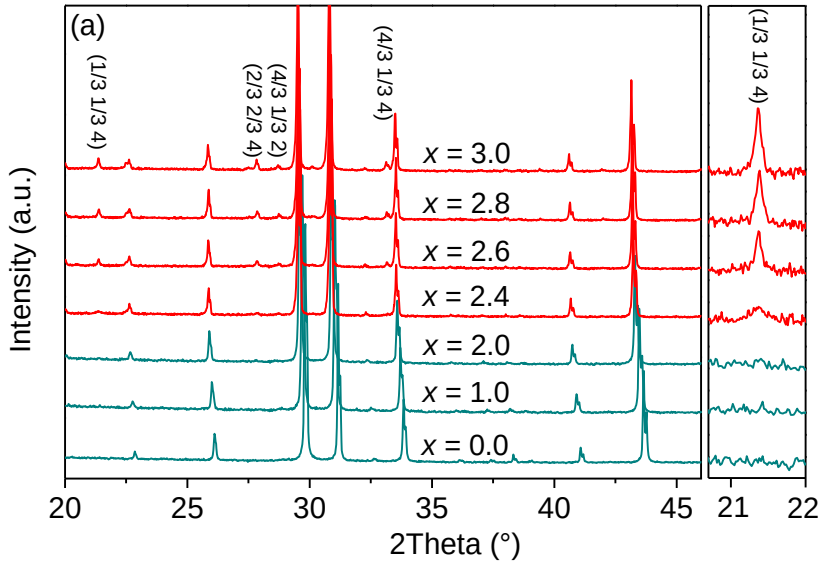

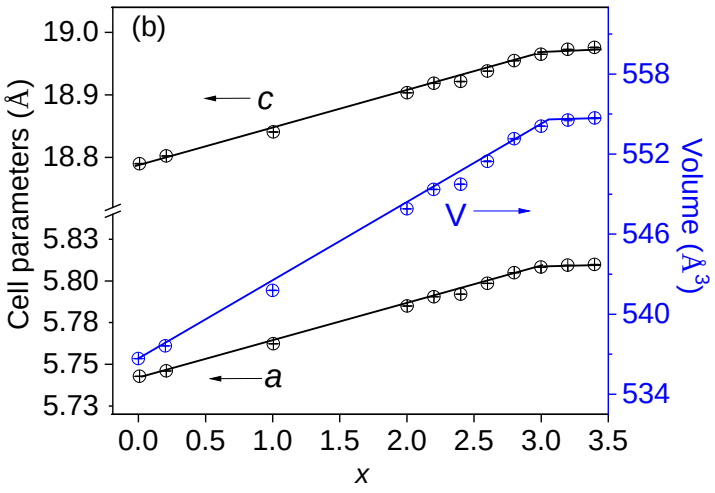

Figure 1. (a) XRPD patterns and (b) refined cell parameters of $Ba_8Cr_{4-x}Ta_{4+0.6x}O_{24}$. The indices of additional reflections of the tripled 8H phase compared with the simple 8H phase in (a) are given based on the unit cell of the simple 8H phase. The insert on the right of (a) enlarges the reflection in 20.7-22° 2Theta range. The *a* axis lengths and volumes for the tripled 8H phases in (b) are respectively divided by $\sqrt{3}$ and 3 for comparison with the simple 8H phases.

Structural analysis of tripled 8H structure. For comparison with $Ba_8MTa_6O_{24}$ (M = Zn, Cu, Co, Mg, Ni)[2, 12-14, 24] and $Ba_8Ga_{4-x}Ta_{4+0.6x}O_{24}$[14], the structural analysis here focuses on the tripled 8H superstructure of $Ba_8Cr_{1.2}Ta_{5.68}O_{24}$ (x = 2.8). The SEM-EDS elemental analysis of $Ba_8Cr_{1.2}Ta_{5.68}O_{24}$ ceramic shows that the composition is essentially homogeneous all over the pellet sample (Figure S2) and led to an average cationic composition of $Ba_8Cr_{1.30(8)}Ta_{5.45(4)}$, close to the nominal composition. The SAED patterns (Figure 2), confirmed the triple unit cell of a ~ 10.07 Å, c ~ 19.01 Å with reflection conditions consistent with the space group $P6_3/mcm$ (No. 193), $P6_3cm$ (No. 185) or $Pc2$ (No. 188) for $Ba_8Cr_{1.2}Ta_{5.68}O_{24}$. Combined Rietveld refinements from XRPD and NPD data (Figure 3) were performed on the $Ba_8Cr_{1.2}Ta_{5.68}O_{24}$ sample data, based on the $P6_3cm$ acentric structural model used for $Ba_8MTa_6O_{24}$[2, 12-14, 24] and $Ba_8Ga_{4-x}Ta_{4+0.6x}O_{24}$[17] cases. The refinements confirm that the B-site vacancies are confined only on the

FSO B sites. However, as there are four crystallographically distinct FSO B sites (B1-3 and B6 sites in Figure 4a) in the *P6$_3$cm* model, refinement of the occupancies of two cations in these partially occupied FSO sites is challenging. Thus similarly to the $Ba_8Ga_{4-x}Ta_{4+0.6x}O_{24}$ case[17], all B site occupancies (including the CSO B4 and B5 sites in Figure 4a) were refined with a simulated annealing approach and under the compositional constrain according to the nominal compositions. The compositional constraint was applied by placing a penalty function on the calculated and nominal overall contents of Cr and Ta based on the sums of atom contents for each type on all of the B sites with the site occupancies and multiplicity taken into consideration. The final refinement shows that the CSO B4 and B5 sites are fully occupied by Ta atoms; the FSO B1 and B2 sites (Figure 4c) comprise respectively 0.62(2) Ta/0.16(5) Cr/0.22 □ (□ represents vacancy) and 0.16(4) Ta/0.73(8) Cr /0.11 □, while the FSO B3 sites consist of 0.95(1) Ta and 0.05(1) Cr, and the FSO B6 sites are empty. The B-site vacancy contents calculated from the site occupancies are consistent with their layer thicknesses: e.g. the empty B6 octahedron exhibits the largest layer thickness (~ 2.74 Å), which is comparable to the layer thickness of the empty B6 octahedron (~ 2.78 Å) in $Ba_8Ga_{0.8}Ta_{5.92}O_{24}$[17] as their oxygen ions are bound with one B cation and pulled toward the neighboring FSO cations on B3 and B4 sites; the layer thicknesses of FSO B1 and B2 octahedrons containing ~ 10-20% vacancies are respectively ~ 2.42 Å and ~ 2.46 Å, which are larger than that of FSO B3O$_6$ (~ 2.24 Å), CSO B4O$_6$ (~ 2.32 Å) and CSO B5O$_6$ (~ 2.25 Å) octahedra with fully occupied B sites. The calculated BVSs of Cr/Ta at the fully-occupied B3, B4 and B5 sites are close to the expected ones for Cr^{3+}/Ta^{5+}. While the BVSs of Cr/Ta at B1 (2.74/4.65) and B2 (2.54/4.32), are essentially consistent with the oxidation states for Cr^{3+}/Ta^{5+}. The slightly lower values than the expected ones are ascribed to the partial occupation at the B1 and B2 sites. The refinement converged to R_{wp} ~ 4.15 % and R_p ~ 2.88 %

for XRPD data (Figure 3a) and R_{wp} ~ 4.03 % and R_p ~ 3.18 % for NPD data (Figure 3b). The final refined structural parameters and bond lengths for $Ba_8Cr_{1.2}Ta_{5.68}O_{24}$ are listed in table 1 and 2, respectively.

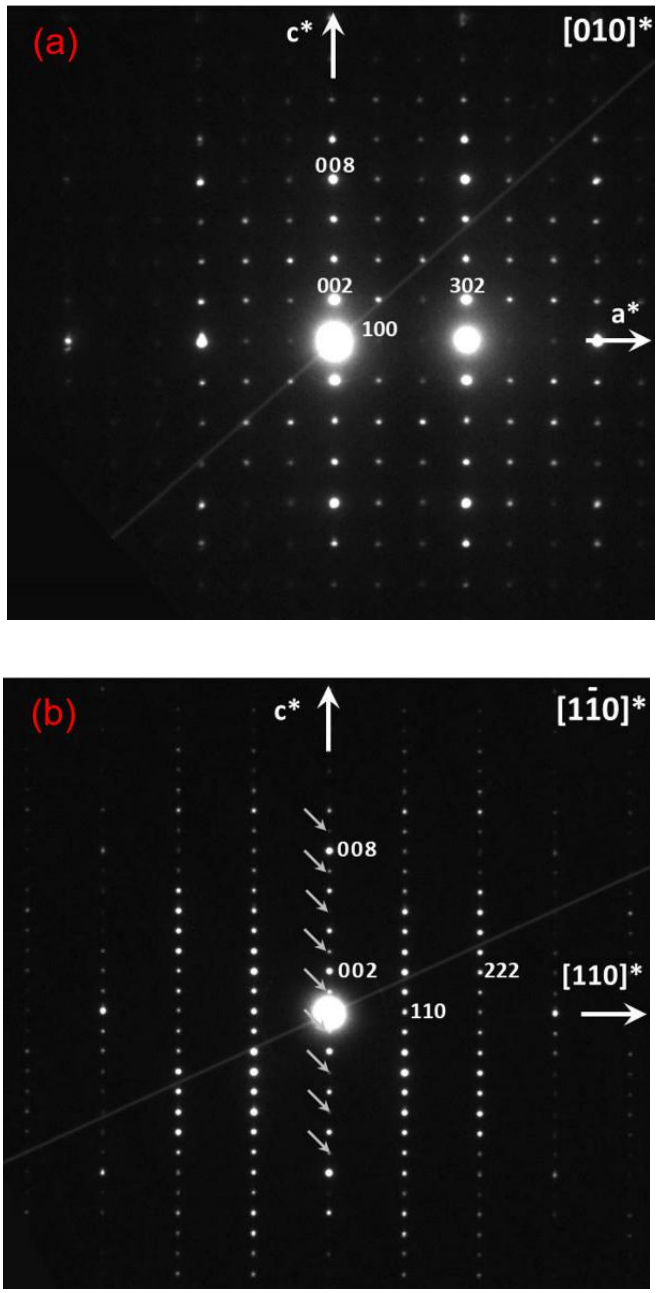

Figure 2. SAED patterns of the $Ba_8Cr_{1.2}Ta_{5.68}O_{24}$ composition recorded along (a) [010] and (b) [1$\bar{1}$0] directions. The small arrows in (b) denote reflections due to double diffraction effect.

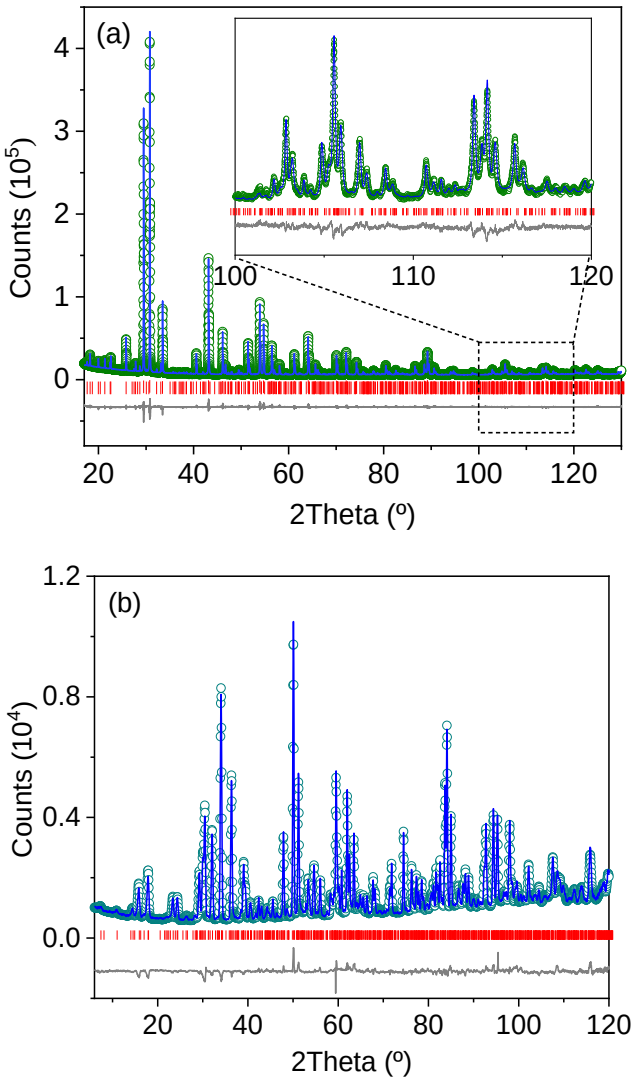

Figure 3. Rietveld refinement plots of (a) XRPD data and (b) NPD data of $Ba_8Cr_{1.2}Ta_{5.68}O_{24}$. The insert in (a) enlarges the plot in the 2Theta range of 100 – 120 °.

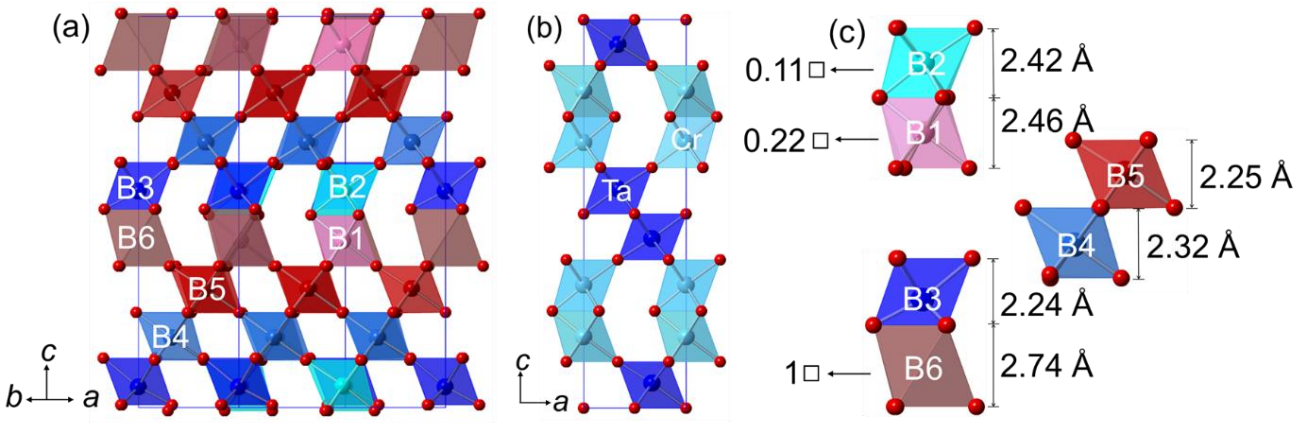

Figure 4. Crystal structure plots of (a) the tripled 8H $Ba_8Cr_{1.2}Ta_{5.68}O_{24}$ with six B sites B1, B2, B3, B4, B5 and B6 labelled in comparison with (b) the simple 8H Ba_2CrTaO_6. The FSO B1-B2 dimers are occupied by Cr, Ta and vacancy, and the FSO B3 is occupied by Ta and a small number of Cr, CSO B4 and B5 sites are only occupied by Ta while the B6 sites are empty. (c) Layer thicknesses of BO_6 octahedron in the tripled 8H $Ba_8Cr_{1.2}Ta_{5.68}O_{24}$ structure with vacancy contents labelled for B1, B2 and B6 sites.

Table 1. Final refined structural parameters of tripled 8H $Ba_8Cr_{1.2}Ta_{5.68}O_{24}$* in $P6_3cm$ space group from a Rietveld refinement combining XPRD and NPD data.

ato	Site	*x*	*y*	*z*	occupancy	U_{iso}(Å^2)
Ba1	2*a*	0	0	0.25	1	0.34(1)
Ba2	4*b*	1/3	2/3	0.2350(2)	1	0.34(1)
Ba3	6*c*	0.6594(5)	0	0.6034(2)	1	0.34(1)
Ba4	6*c*	0.3100(3)	0	0.8819(3)	1	0.34(1)
Ba5	6*c*	0.3348(7)	0	0.4897(3)	1	0.34(1)
B1	4*b*	1/3	2/3	0.4271(3)	0.62(2) Ta/0.16(5) Cr	0.030(5)
B2	4*b*	1/3	2/3	0.0563(4)	0.16(4) Ta/0.73(8) Cr	0.030(5)
B3	2*a*	0	0	0.0528(1)	0.95(1) Ta/0.05(1) Cr	0.030(5)
B4	6*c*	0.3301(3)	0	0.6786(1)	0.998(6) Ta	0.030(5)

B5	6*c*	0.6638(3)	0	0.8041(1)	0.997(7) Ta	0.030(5)
O1	6*c*	0.5034(4)	0	0.2425(2)	1	0.087(9)
O2	6*c*	0.1868(3)	0.1868(3)	0.8641(2)	1	0.087(9)
O3	6*c*	0.1644(3)	0.1644(3)	0.5080(1)	1	0.087(9)
O4	12*d*	0.6682(4)	0.1804(2)	0.4930(1)	1	0.087(9)
O5	12*d*	0.3347(2)	0.1652(2)	0.2442(1)	1	0.087(9)
O6	12*d*	0.6730(3)	0.1589(3)	0.1217(1)	1	0.087(9)
O7	6*c*	0.1665(4)	0.1665(4)	0.1269(2)	1	0.087(9)
O8	12*d*	0.5082(2)	0.3435(3)	0.8617(1)	1	0.087(9)

* Space group $P6_3cm$ (No. 185), a = 10.01521(2) Å, c = 18.88022(9) Å, and V = 1640.05(1) Å^3, Z = 3.

Table 2. Bond lengths and Bond Valence Sums (BVSs) for the tripled 8H $Ba_8C_{1.2}Ta_{5.68}O_{24}$ structure.

Bond	length (Å)	Bond	length (Å)	bond	length (Å)
Ba1 – O2 (×3)	2.853(4)	Ba4 – O2 (×2)	2.728(4)	B1 – O4 (×3)	1.979(4)
Ba1 – O5 (×6)	2.905(2)	Ba4 – O4 (×2)	2.847(5)	B1 – O8 (×3)	2.053(4)
Ba1 – O7 (×3)	2.861(4)	Ba4 – O3 (×1)	2.792(6)	$(BVS)_{Cr/Ta}$ at B1	2.74/4.65
$(BVS)_{Ba1}$	2.38	Ba4 – O8 (×2)	3.015(3)	B2 – O4 (×3)	1.949(6)
Ba2 – O8 (×3)	2.901(4)	Ba4 – O8 (×2)	3.031(3)	B2 – O6 (×3)	2.166(5)
Ba2 – O6 (×3)	2.783(4)	Ba4 – O5 (×2)	3.047(5)	$(BVS)_{Cr/Ta}$ at B2	2.54/4.32
Ba2 – O5 (×3)	2.885(2)	Ba4 – O1 (×1)	3.228(6)	B3 – O3 (×3)	1.851(3)
Ba2 – O1 (×3)	2.895(3)	$(BVS)_{Ba4}$	2.17	B3 – O7 (×3)	2.177(4)
$(BVS)_{Ba2}$	2.52	Ba5 – O2 (×1)	2.796(7)	$(BVS)_{Cr/Ta}$ at B3	3.01/5.11
Ba3 – O3 (×1)	2.522(5)	Ba5 – O3 (×2)	2.925 (7)	B4 – O7 (×1)	1.907(5)
Ba3 – O4 (×2)	2.731(4)	Ba5 – O4 (×2)	2.881(2)	B4 – O6 (×2)	1.907(3)
Ba3 – O6 (×2)	2.863(3)	Ba5 – O4 (×2)	2.896(7)	B4 – O5 (×2)	2.083(3)

Ba3 – O6 (×2)	2.905(6)	Ba5 – O8 (×2)	2.952(5)	B4 – O1 (×1)	2.058(5)
Ba3 – O7 (×2)	2.988(6)	Ba5 – O6 (×2)	2.937(6)	$(BVS)_{Ta}$ at B4	5.07
Ba3 – O1 (×1)	3.091(6)	Ba5 – O7 (×1)	3.091(7)	B5 – O2 (×1)	1.877(5)
Ba3 – O5 (×2)	3.147(4)	$(BVS)_{Ba5}$	2.18	B5 – O8 (×2)	2.007(3)
$(BVS)_{Ba3}$	2.53			B5 – O1 (×1)	2.039(4)
$(BVS)_{O1}$ [a]	1.99	$(BVS)_{O5}$ [a]	2.03	B5 – O5 (×2)	2.010(3)
$(BVS)_{O2}$ [a]	2.19	$(BVS)_{O6}$ [a]	2.19	$(BVS)_{Ta}$ at B5	5.00
$(BVS)_{O3}$ [a]	2.32	$(BVS)_{O7}$ [a]	2.15		
$(BVS)_{O4}$ [a]	2.06	$(BVS)_{O8}$ [a]	1.91		

[a] The site occupancies of Cr/Ta at B sites were considered in the BVS calculation for oxygen atoms.

STEM-HAADF imaging of $Ba_8Cr_{1.2}Ta_{5.68}O_{24}$. Local B-site cationic distribution in $Ba_8Cr_{1.2}Ta_{5.68}O_{24}$ was observed by STEM-HAADF imaging at the atomic resolution level. Since the contrast in STEM-HAADF images is proportional to the sample density and the atomic number Z of the elements, for the observed thin area (several tens of nanometers thick), an analytical expression of the Z dependence of the image intensity can be approximated by $I \propto Z^n$ with n in the range 1.6 – 2. At the atomic scale, for an atomic column composed of several elements (i) with a ratio m_i and Z_i (the atomic number of the element i), this formula becomes $I \propto \sum_i (m_i Z_i^n)$. Consequently, intensity profiles can be used to analyze the elemental atomic distribution by indexing the atomic columns from the brightest to the darkest contrasts in relation with the heaviest to the lightest atom sites: B4-B5: Ta (Z = 73) > Ba (Z = 56) > B_1:Ta_1 (≈ 49) > B_2:Ta_2 (≈ 29). Figure 5a shows STEM-HAADF image recorded along the [010] direction to obtain the atomic information along all the atomic columns, and the intensity profiles of three typical strips from the STEM-HAADF image for $Ba_8Cr_{1.2}Ta_{5.68}O_{24}$. The probe with the

smallest size was used considering the short distances of Ba-Ba (2.4 Å) and Ba-Ta1/Ta2 (1~1.2 Å) along the *c* axis in the projected plane. Variation of local cation distribution in the sample may be indirectly demonstrated by the intensity profiles (Figure 5b) within one cell along the stacking direction of the BaO_3 layer, i.e. the *c* axis. The intensity dropping on B sites located at the same layer along the *c* axis (highlighted by the red arrows in Figure 5b) indicates that the corresponding B sites are co-occupied with Cr or vacancies. Accordingly, the intensity from site to site of the same B-cation layer may vary along the c axis, depending on the local distribution of Cr and vacancy along the b axis. The EDS atomic maps of Ba/Ta (Figure S3) was also attempted to confirm the cationic distribution proposed from the intensity profiles. The resolution of the EDS mapping does not enable atomic resolution given the short distances between the atomic columns (Ba-Ba (2.4 Å) and Ba-Ta1/Ta2 (1~1.2 Å) along the *c* axis), and the sample drift caused by the electron discharging process. Although Cr atoms cannot be detected due to their low content and relatively low atomic number, fortunately, Ba atoms can be clearly distinguished and the Ta distribution can be discerned. Two areas can be identified: the CSO Ta4-Ta5 blocks and the FSO blocks with less Ta distribution marked in blue and red region, respectively in Figure S3, confirming the existence of B-site vacancy and Cr atoms within the FSO sites.

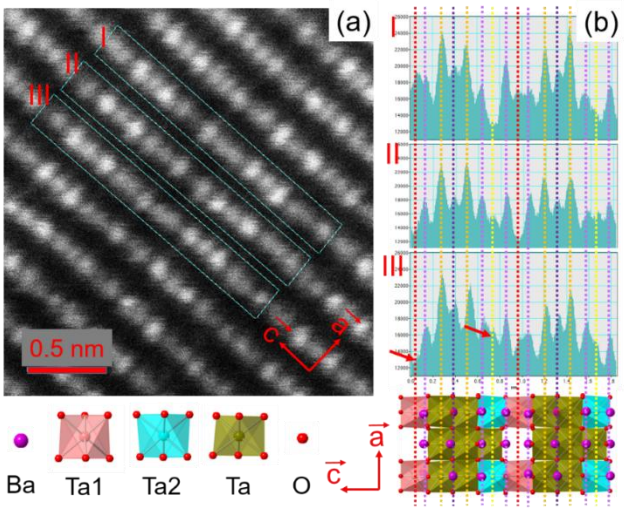

Figure 5. (a) STEM-HAADF image for $Ba_8Cr_{1.2}Ta_{5.68}O_{24}$ along the [010] orientation and (b) extracted intensity profiles of three typical strips highlighted by green rectangles in (a). The red arrows in the intensity profiles mark different atom contents at the B sites in the same layer along the *c* axis.

XPS data. The oxidation states of chromium in the as-made and low-temperature annealed (800 °C in air for 6 h) $Ba_8Cr_{4-x}Ta_{4+0.6x}O_{24}$ (x = 0, 2.8) powders were examined by XPS measurements. Although no difference from the XRPD patterns between the as-made and air-annealed samples (Figure S4) could be detected, their XPS spectra (Figure 6) exhibit different features. For the as-made samples, the $2p_{3/2}$ and $2p_{1/2}$ peaks centered at 575.3 eV and 584.8 eV for the x = 0 composition, and at 576.7 eV and 586.6 eV for the x = 2.8 composition are assigned to Cr^{3+}. Apart from these two peaks, there are additional peaks around 578.8 eV for Ba_2CrTaO_6 or 579.6 eV for $Ba_8Cr_{1.2}Ta_{5.68}O_{24}$, belonging to Cr^{6+} $2p_{3/2}$ line[27-29], of which intensities increased after the annealing process. This indicates that oxidation from Cr^{3+} to Cr^{6+} took place slightly in the as-made samples during the cooling procedure, which was enhanced significantly upon the low temperature air annealing.

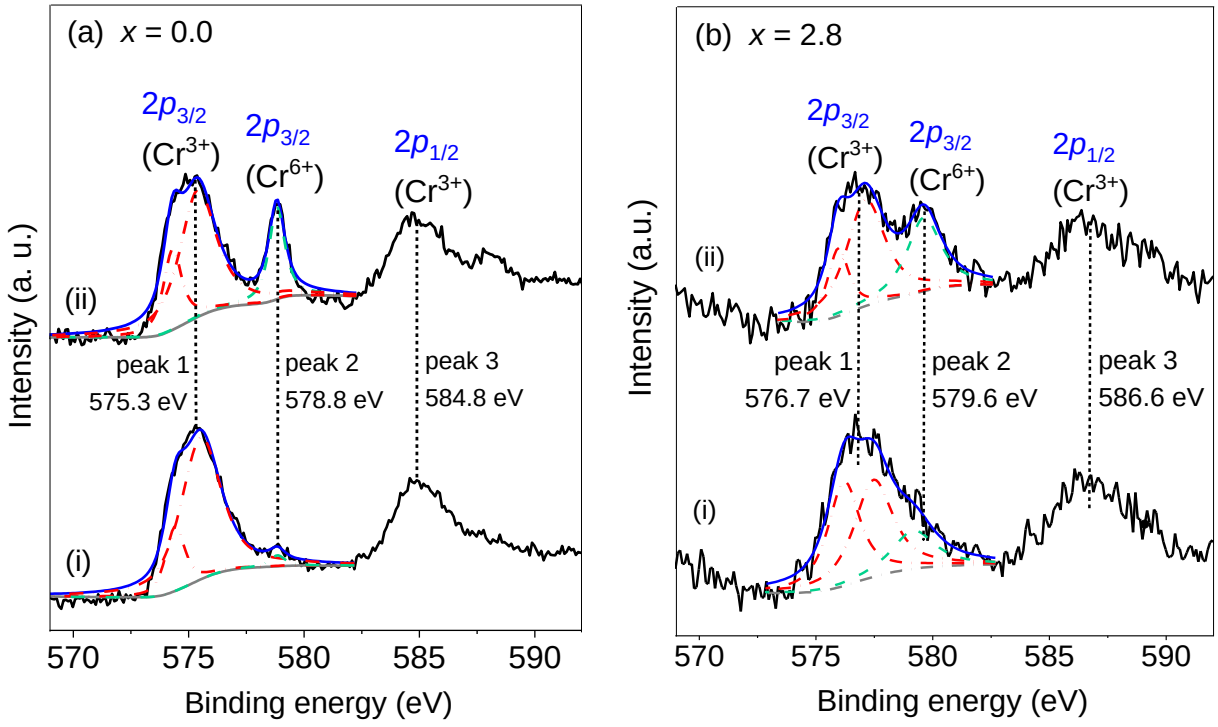

Figure 6. XPS spectra of (a) Ba_2CrTaO_6 and (b) $Ba_8Cr_{1.2}Ta_{5.68}O_{24}$. (i) and (ii) are respectively collected from the as-made and air-annealed samples. The black and blue solid lines represent the experimental and fitted spectra, respectively. The red and green dash lines denote deconvolution into $2p_{3/2}$ lines of Cr^{3+} and Cr^{6+} states, respectively.

Impedance data. AC impedance spectroscopy measurements were performed under N_2 atmosphere for minimizing the oxidation from Cr^{3+} to Cr^{6+}. Figure 7a shows a typical complex impedance plot measured on the tripled 8H sample x = 2.8 at 250 °C. The small and large semicircular arcs have associated capacitances with a magnitude of ~ 3 pF/cm and ~ 10^{-9} F/cm (Figure S5), corresponding to bulk and grain boundary responses, respectively.[30] The bulk and grain boundary response arcs remain well-resolved until the temperature was elevated to 800 °C. The Arrhenius plots of conductivities of $Ba_8Cr_{4-x}Ta_{4+0.6x}O_{24}$ (Figure 7b and S6) show that the

Ta^{5+} substitution for Cr^{3+} decreased the conductivity: the bulk conductivities of $Ba_8Cr_{1.2}Ta_{5.68}O_{24}$ are ~ 2-3 orders of magnitude lower than those of Ba_2CrTaO_6.

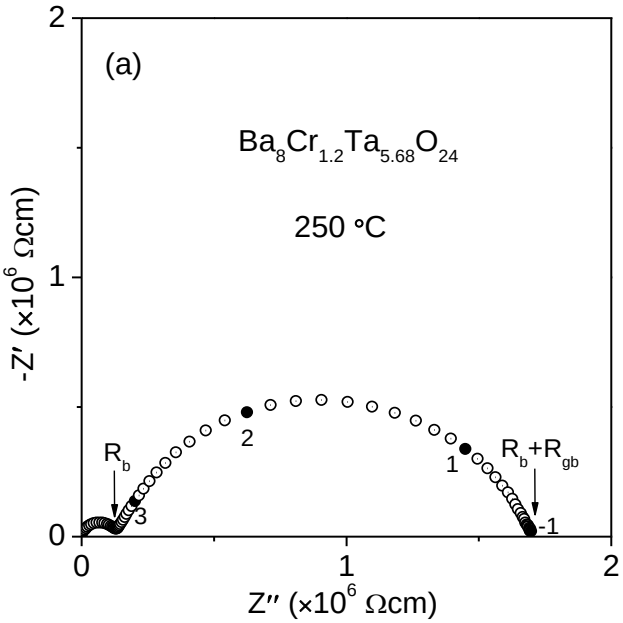

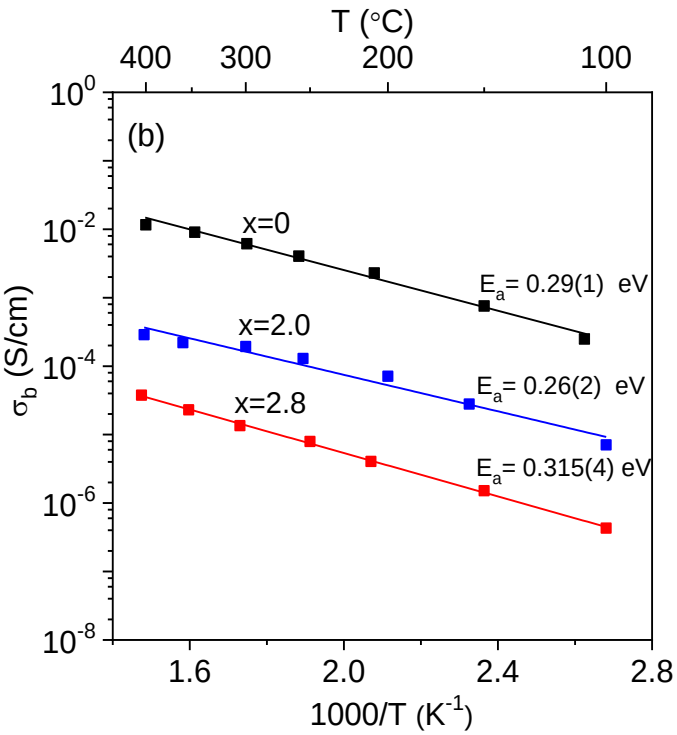

Figure 7. (a) Complex impedance plot of $Ba_8Cr_{1.2}Ta_{5.68}O_{24}$ pellet collected at 250 °C. The numbers represent the logarithm values of the selected frequencies highlighted by the black filled circles. R_b and R_{gb} denotes the resistivities of bulk and grain boundary, respectively. (b) Arrhenius plots of bulk conductivities for $Ba_8Cr_{4-x}Ta_{4+0.6x}O_{24}$ (x = 0.0, 2.0 and 2.8) ceramics.

Microwave dielectric properties. Table 3 shows the microwave dielectric properties and relative densities of the $Ba_8Cr_{4-x}Ta_{4+0.6x}O_{24}$ (x = 0.0-3.0) pellets with relative densities ~ 89-96%. The pellets for the compositions x = 0.0 and 1.0 did not show resonant peaks, indicating high dielectric loss, and the other pellets display modest dielectric permittivity ε_r ~ 25, low Qf values from 4424 to 15985 GHz and large temperature coefficient of resonant frequencies τ_f ~ 14-25 ppm/°C.

Table 3. Microwave dielectric properties and relative densities of $Ba_8Cr_{4-x}Ta_{4+0.6x}O_{24}$ (x = 0.0-3.0) pellets.

composition (x)	ε_r	Qf (GHz)	τ_f (ppm/°C)	relative density (%)
0.0	--	--	--	91
1.0	--	--	--	92
2.0	25	4424	14	96
2.4	25	15985	25	96
2.6	25	5816	18	92
2.8	25	7698	20	89
3.0	25	10947	15	91

Microstructure. The surface morphology images recorded by SEM on pellets of x = 0.0-3.0 compositions show that the pellets contain plate-shaped grains with thickness ~ 2 μm which are tightly packed (Figure 8). The grain sizes (width and length) in the compositions x = 0.0 and 2.0 have broad distribution up to ~ 10 μm. While the Ta-rich compositions display some extraordinary long grains (> 40 μm).

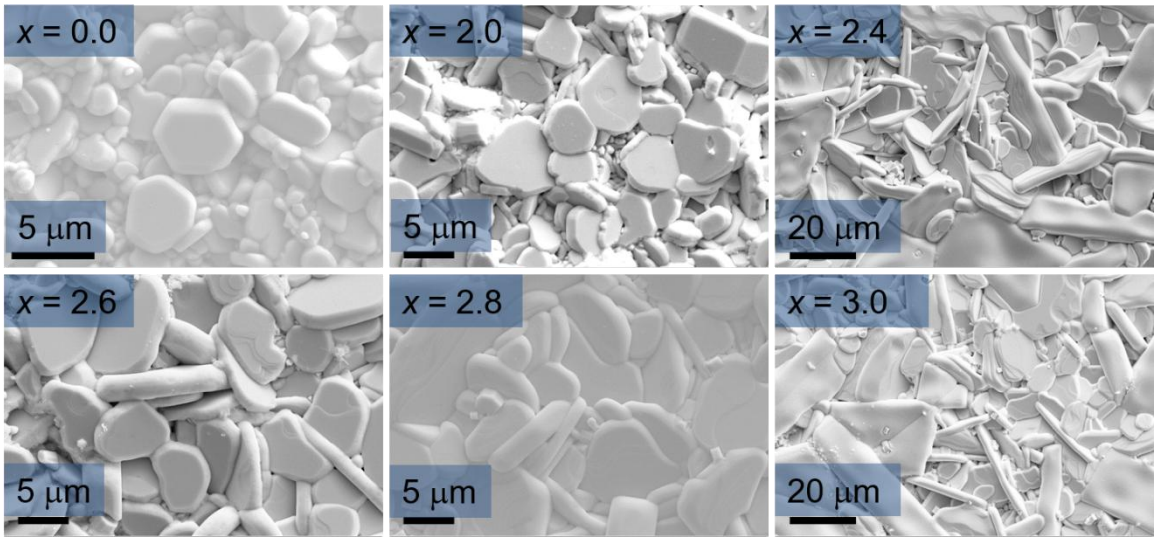

Figure 8. SEM images of $Ba_8Cr_{4-x}Ta_{4+0.6x}O_{24}$ (x = 0.0-3.0) compositions.

◘ DISCUSSION

Stabilization of the 8-layer twinned structure. The 8-layer twinned hexagonal perovskites are usually line phase with either fully occupied B-sites or partially occupied B-sites with fixed vacancy content at 12.5%. Only two exceptions have been reported, namely $Ba_8Ga_{4-x}Ta_{4+0.6x}O_{24}$[17] and $Ba_8Ta_{4+0.8x}Ti_{3-x}O_{24}$[18] showing variable B-site vacancy contents as ~ 10-16% and 12.5-14.5%, respectively. The $Ba_8Cr_{4-x}Ta_{4+0.6x}O_{24}$ solid solution reported here shows the widest B-site vacancy content range (0-15%) among the 8-layer twinned hexagonal perovskites. The end member Ba_2CrTaO_6[19, 31] , containing two distinguished occupation blocks for Cr (in

FSO dimers) and Ta (in CSO dimers), features covalent Cr-Cr and 90° Cr-O-Cr bonding in the FSO dimers. According to Goodenough[32], the covalency of these metal-metal and metal-anion-metal bonding are enhanced via respectively forming σ bonds between the t_{2g} orbits of transitional metal cations and $\sigma - \pi$ bonds between the t_{2g} orbits of transitional metal cations and the 2*p* orbits of oxide anions. The certain Cr/Ta atomic ratio and bonding solution therefore are deemed to be the main reason for the stabilization of the *B*-site fully occupied 8-layer twinned hexagonal structure. In $Ba_8Cr_{4-x}Ta_{4+0.6x}O_{24}$ ($x \neq 0$), the aliovalent substitution of Ta^{5+} for Cr^{3+} induces B-site vacancies, therefore both Cr-Cr and Cr-O-Cr bonding, and B-site vacancies as well as cation ordering in the FSO sites could contribute together to the stabilization of the $Ba_8Cr_{4-x}Ta_{4+0.6x}O_{24}$ twinned hexagonal perovskite structure. The FSO Cr-Cr and Cr-O-Cr bonding still takes place in Ta-rich compositions as there are still ~ 16% FSO Cr–Cr dimers in the $Ba_8Cr_{1.2}Ta_{5.68}O_{24}$ composition among the FSO B1-B2 dimers (the rest are ~ 33% Ta/Cr–□, ~ 51% Ta–Cr dimers for minimizing the B-B repulsion) according to the structure refinement (Table 1). Although there are large amount of ~ 51% Ta–Cr in the FSO B1-B2 dimers, the average B1-B2 distance (~ 2.46 Å) in $Ba_8Cr_{1.2}Ta_{5.68}O_{24}$ is essentially identical to the Cr-Cr distance (~ 2.49 Å) in Ba_2CrTaO_6. This could be mainly ascribed to the existence of vacancies in the FSO B1-B2 dimers. As indicated by the formation of simple and tripled 8H structures respectively within $0 \leq x < 2.4$, and $2.4 \leq x \leq 3.0$ ranges, the covalent Cr-Cr and Cr-O-Cr bonding could play a dominant role within $0.0 \leq x < 2.4$, while the B-site vacancies and cation ordering could take over the Cr-Cr and Cr-O-Cr bonding in the Ta-rich range $2.4 \leq x \leq 3.0$. High dilution of Cr atoms, ordering of Cr/Ta atoms and vacancies are required to minimize the FSO electrostatic repulsion through avoiding formation of the Ta^{5+}-Ta^{5+} dimers. The accommodation of partial ordered vacancies and cations in the FSO B sites is helpful to relieve the FSO B–B

repulsion, which is common in twinned hexagonal perovskite structures, i.e. 8-layer $Ba_8ZnTa_6O_{24}$[12] and $Ba_8Ti_3Ta_4O_{24}$[33], 10-layer $Ba_{10}Ti_{1.2}Ta_{7.04}O_{30}$[33] and $Ba_8Zr_{0.4}Ti_{2.6}Ta_4O_{24}$[34], and 14-layer $Ba_{14}Mn_{1.75}Ta_{10.5}O_{42}$[7] as well as the shifted hexagonal structures with completely ordered vacant octahedral layer between two successive *h* layers.

Dielectric loss. Similarly to the $Ba_8Ga_{4-x}Ta_{4+0.6x}O_{24}$ case, a tendency of the less Cr content or the higher B-site vacancy content, the higher Q*f* values[18] was observed for $Ba_8Cr_{4-x}Ta_{4+0.6x}O_{24}$ compositions. It is interesting to note there is an exception for x = 2.4 at the critical point of disorder-order transition showing the highest Q*f* value among $Ba_8Cr_{4-x}Ta_{4+0.6x}O_{24}$, which is not well understood and awaits further investigation. Compared with $Ba_4LiTa_3O_{24}$[35], $Ba_8Ga_{4-x}Ta_{4+0.6x}O_{24}$[17], $Ba_8Ti_{3-x}Ta_{4+0.8x}O_{24}$[18] and $Ba_8MTa_6O_{24}$ (M = Co, Ni, Zn)[2, 12-14] cases, $Ba_8Cr_{4-x}Ta_{4+0.6x}O_{24}$ pellets possess much lower Q*f* values. Such high dielectric loss of $Ba_8Cr_{4-x}Ta_{4+0.6x}O_{24}$ could be attributed to the existence of Cr^{3+} with partially filled *d* shells and cationic disorder in the structure as well as inhomogeneous microstructure. The resonant spin excitation induced by the unpaired d electrons in transition metal atoms can be attributed to the microwave dielectric loss, which could explain the high microwave dielectric loss of $Ba(Zn_{1/3}Ta_{2/3})O_3$[36] and $Ba_8MnNb_6O_{24}$[37], as well as the materials in this work. On the other hand, owing to the smaller charge and size differences between Cr^{3+} (0.615 Å) and Ta^{5+} (0.64 Å)[26] compared with those between M^{2+} (M = Ni, Mg, Cu, Co, Zn, 0.69-0.72 Å) and Ta^{5+}, the distribution of Cr/Ta atoms and vacancies in the FSO sites is much more disordered than in $Ba_8MTa_6O_{24}$. This could be the main reason of the higher Q*f* values for $Ba_8MTa_6O_{24}$ (M = Co, Ni, Zn) although Co^{2+} and Ni^{2+} ions have also partially filled d orbits and unpaired electrons.

Regarding the inhomogeneous microstructure, it is interesting to compare the Ta-rich composition $Ba_8Cr_{1.2}Ta_{5.68}O_{24}$ with $Ba_8CuTa_6O_{24}$[38] regarding their comparable Q*f* values as well

as their more insulating grain boundary regions than grains. In $Ba_8CuTa_6O_{24}$, there is partial reduction from Cu^{2+} to Cu^{+} during the firing procedure and limited reoxidation along the grain boundary region on cooling, therefore enhancing the resistivity for the grain boundary. In $Ba_8Cr_{4-x}Ta_{4+0.6x}O_{24}$, as revealed by XPS measurements, partial oxidation of Cr^{3+} into Cr^{6+} could take place unavoidably on cooling. This is expected to induce p type conduction, which was confirmed by the bulk conductivity measured as a function of partial oxygen pressure in Ba_2CrTaO_6 (x = 0.0) (Figure S7). Therefore, if partial oxidation of Cr^{3+} into Cr^{6+} took place along the grain boundary, smaller resistivity would be measured for the grain boundary regions compared to the grains. However, this is in contradiction with experimental observations. As the XPS technique detects only the surface, the partial oxidation of Cr^{3+} to Cr^{6+} could not take place as bulk property. Careful SEM-EDS elemental mapping at higher magnification on the $Ba_8Cr_{1.2}Ta_{5.68}O_{24}$ pellet revealed the existence of small amount of Ta-rich oxide phases different from the main phase along the boundary regions (Figure S8), which could explain the more insulating grain boundary compared to the grains. The electrically and compositional inhomogeneous (along grain boundary regions) microstructure in $Ba_8Cr_{4-x}Ta_{4+0.6x}O_{24}$ pellets could also contribute to their high microwave dielectric losses.

◘ CONCLUSION

Aliovalent substitution of Ta^{5+} for Cr^{3+} in the B-site fully occupied hexagonal perovskite Ba_2CrTaO_6 led to an 8-layer twinned hexagonal solid solution $Ba_8Cr_{4-x}Ta_{4+0.6x}O_{24}$ showing the widest B-site vacancy content range reported to date (0-15%). $Ba_8Cr_{4-x}Ta_{4+0.6x}O_{24}$ form a simple 8-layer hexagonal perovskite structure within $0.0 \leq x < 2.4$, and a tripled 8-layer hexagonal perovskite superstructure within $2.4 \leq x \leq 3.0$ owing to the partial FSO B cation ordering in the *ab* plane. Complementary techniques including neutron and X-ray powder diffractions as well as

STEM-HAADF imaging and intensity profile analysis confirm the distribution of vacancies in the FSO blocks in the tripled superstructure. The 8-layer twinned hexagonal perovskites $Ba_8Cr_{4-x}Ta_{4+0.6x}O_{24}$ with a broad solid solution range reported here highlight the roles of the covalent Cr-Cr and Cr-O-Cr bonding and the B-site vacancies as well as the cation ordering in the FSO dimers on relieving the electrostatic repulsion and therefore stabilizing the twinned hexagonal perovskite structures.

Supporting information: XRPD patterns of $Ba_8Cr_{4-x}Ta_{4+0.6x}O_{24}$ ($3.2 \leq x \leq 4.0$) compositions; SEM-EDS elemental mapping and STEM-EDS atomic maps of $Ba_8Cr_{1.2}Ta_{5.68}O_{24}$; XRD patterns of $Ba_8Cr_{4-x}Ta_{4+0.6x}O_{24}$ (x = 0.0, 2.8) before and after annealing at 800 °C in Air; Frequency dependency of capacitance for $Ba_8Cr_{1.2}Ta_{5.68}O_{24}$ at 250 °C; Total conductivities for $Ba_8Cr_{4-x}Ta_{4+0.6x}O_{24}$ (x = 0.0, 2.8); The pO_2 dependency of the bulk conductivity for Ba_2CrTaO_6 at 400 °C. CSD 2049793 contains the supplementary crystallographic data for this paper. These data can be obtained free of charge from The Cambridge Crystallographic Data Centre via www.ccdc.cam.ac.uk/structures.

ACKNOWLEDGEMENT

The National Nature Science Foundation of China (Nos. 22090043, 2136008 and 21511130134), Guangxi Natural Science Foundation (No. 2019GXNSFGA245006), Guangxi Program for Hundred Talents for Returned Scholars, Key Laboratory of New Processing Technology for Nonferrous Metal & Materials, Ministry of Education/ Guangxi Key Laboratory of Optical and Electronic Materials and Devices (20AA-1), as well as CNRS (bilateral TransLight project, PICS07091) are acknowledged for financial support. TEM results were realized through the project of Région-Centre Val de Loire and the French minister of research (MESRI – DRRT)

and Centre-Val de Loire region with the European regional development fund (ERDF) which are co-funded by Europe Union. The authors acknowledge the ICMN laboratory (Orléans, France) for TEM (CM20) access. Prof. Liang Fang and Prof. Huanfu Zhou are acknowledged for access to the microwave dielectric measurements.

◘ REFERENCES

1. Kuang, X.; Allix, M. M. B.; Claridge, J. B.; Niu, H.; Rosseinsky, M. J.; Ibberson, R. M.; Iddles, D. M. Crystal structure, microwave dielectric properties and AC conductivity of B-cation defficient hexagonal perovskite $La_5M_xTi_{4-x}O_{15}$ (x = 0.5, 1; M = Zn, Mg, Ga. Al). *J. Mater. Chem* **2006,** 16, 1038-1045.

2. Moussa, S. M.; Clarige, J. B.; Rosseinsky, M. J.; Clark, S. $Ba_8ZnTa_6O_{24}$: a high-Q microwave dielectric from a potentially diverse homologous series. *Appl. Phys. Lett.* **2003,** 82, 4537-4539.

3. Keith, G. M.; A., K. C.; Sarma, K.; Alford, N. M.; Cussen, E. J.; Rosseinsky, M. J.; Sinclair, D. C. Synthesis, crystal structure, and characterization of $Ba(Ti_{1/2}Mn_{1/2})O_3$: a high pernittivity 12R-type hexagonal perovskite. *Chem. Mater.* **2004,** 16, 2007-2015.

4. Kuang, X.; Bridges, C.; Allix, M.; Claridge, J. B.; Hughes, H.; Rosseinsky, M. J. Internal barrier layer capacitance effect in hexagonal perovskite $Ba_4YMn_3O_{11.5}$. *Chem. Mater.* **2006,** 18, 5130-5136.

5. Kuang, X.; Allix, M.; Ibberson, R. M.; Claridge, J. B.; Niu, H.; Rosseinsky, M. J. Oxygen vacancy ordering phenomena in the mixed-conducting hexagonal perovskite $Ba_7Y_2Mn_3Ti_2O_{20}$. *Chem. Mater.* **2007,** 19, 2884-2893.

6. Fop, S.; Skakle, J.; McLaughlin, A. C.; Connor, P. A.; Irvine, J. T. S.; Smith, R. I.; Wildman, E. J. Oxide ion conductivity in the hexagonal perovskite derivative $Ba_3MoNbO_{8.5}$. *J. Am. Chem. Soc.* **2016,** 138, 16764-16769.

7. Tao, F.; Genevois, C.; Lu, F.; Kuang, X.; Porcher, F.; Li, L.; Yang, T.; Li, W.; zhou, D.; Allix, M. First 14-layer twinned hexagonal perovskite $Ba_{14}Mn_{1.75}Ta_{10.5}O_{42}$: atomic-scale imaging of cation ordering. *Chem. Mater.* **2016,** 28, 4686-4696.

8. Xu, T.; Zhang, C.; Shao, X.; Wu, K.; Zhu, Y. Monomolecular-layer $Ba_5Ta_4O_{15}$ nanosheets: synthesis and investigation of photocatalytic properties. *Adv. Funct. Mater.* **2006,** 16, 1599-1607.

9. Yugo, M.; Hideki, K.; Akihiko, K. Water spliting into H_2 and O_2 over niobate and titanate photocatalysts with (111) plane-type layered perovskite structure. *Energy Environ. Sci.* **2009,** 2, 306-314.

10. Trolliard, G.; Ténèwe, N.; Boullay, P.; Mercurio, D. TEM study of cation-deficient-perovskite related $A_nB_{n-1}O_{3n}$ compounds: the twin-shift option. *J. Solid State Chem.* **2003,** 177, 1188-1196.

11. Kuroda, K.; Ishizawa, N.; Mizutani, N.; Kato, M. The crystal structure of α-$SrMnO_3$. *J. Solid State Chem.* **1981,** 38, 297-299.

12. Thirumal, M.; Davies, P. K. $Ba_8ZnTa_6O_{24}$: a new high Q dielectric perovskite. *J. Am. Ceram. Soc* **2005,** 88, 2126-2128.

13. Kan, A.; Ogawa, H.; Yokoi, A.; Ohsato, H. Microwave dielectric properties of perovskite-like structure $Ba_8Ta_6(Ni_{1-x}M_x)O_{24}$ (M = Co, Cu and Zn) solid solution. *Jpn. J. Appl. Phys* **2006,** 45, 7494-7498.

14. Kawaguchi, S.; Ogawa, H.; Kan, A.; Ishihara, S. Microwave dielectric properties of $Ba_8Ta_6(Ni_{1-x}M_x)O_{24}$ (M = Zn and Mg) ceramics. *J. Eur. Ceram. Soc.* **2006,** 26, 2045-2049.

15. Guo, H.; Zhou, D.; Du, C.; Wang, P.; Liu, W.; Pang, L.; Wang, Q.; Su, J.; Singh, C.; Trukhanov, S. Temperature stable $Li_2Ti_{0.75}(Mg_{1/3}Nb_{2/3})_{0.25}O_3$-based microwave dielectric ceramics with low sintering temperature and ultra-low dielectric loss for dielectric resonator antenna applications. *J. Mater. Chem. C* **2020,** 8, 4690-4700.

16. Guo, H.; Fu, M.; Zhou, D.; Du, C.; Wang, P.; Pang, L.; Liu, W.; Sombra, A. S. B.; Su, J. Design of a high-efficiency and -gain untenna using novel low-loss, temperature-stable $Li_2Ti_{1-x}(Cu_{1/3}Nb_{2/3})_xO_3$ microwave dielectric ceramics. *ACS Appl Mater Interfaces* **2021,** 13, 912-923.

17. Cao, J.; Kuang, X.; Allix, M.; Dickinson, C.; Claridge, J. B.; Rosseinsky, M. J.; Iddles, D. M.; Su, Q. New 8-layer twinned hexagonal perovskite microwave dielectric ceramics $Ba_8Ga_{4-x}Ta_{4+0.6x}O_{24}$. *Chem. Mater.* **2011,** 23, 5058-5067.

18. Baranov, A. N.; Oh, Y. Microwave frequency dielectric properties of hexagonal perovskite in the $Ba_5Ta_4O_{15}$-$BaTiO_3$ system. *J. Eur. Ceram. Soc.* **2005,** 25, 3451-3457.

19. Choy, J.; Hong, S.; Park, J.; Kim, D. Crystal structure and the role of covalency in eight-layered hexagonal Ba_2CrTaO_6. *Jpn. J. Appl. Phys.* **1993,** 32, 4628-4634.

20. Rietveld, H. M. A profile refinement method for nuclear and magnetic structures. *J. Appl. Crystallogr.* **1968,** 2, 65-71.

21. Coelho, A. A. Topas academic V5; coelho software: Brisbane, Australia. **2012**.

22. Brown, I. D.; Altermatt, D. Bond-valence parameters obtained from a systematic analysis of the inorganic crystal structure database. *Acta Cryst. Section B: Cryst. Struct. Sci.* **1985,** 41, 244-247.

23. Hakki, B. W.; Coleman, P. D. A dielectric resonator method of measuring inductive capacities in the millimeter range. *IEEE Trans. Microwave Theory Tech.* **1960,** 8, 402-410.

24. Abakumov, A. M.; Tendeloo, G. V.; Scheglov, A. A.; Shpanchenko, R. V.; Antipov, E. V. The crystal ctructue of $Ba_8Ta_6NiO_{26}$: cation ordering in hexagonal perovskite. *J. Solid State Chem.* **1996,** 125, 102-107.

25. Denton, A. R.; Ashcroft, N. W. Vegard's law. *Phys. Rev. A.* **1991,** 43, 3161-3164.

26. Shannon, R. D. Revised effective ionic radii and systematic studies of interatomic distances in halides and chalcogenides. *Acta Crystallogr., Sect. A: Found. Crystallogr.* **1976,** 32, 751-767.

27. Contarini, S.; Aduru, S.; Rabalais, J. W. Decomposition of chromate salts stimulated by and electron irradiation. *J. Phys. Chem.* **1986,** 90, 3202-3205.

28. Naumkin, A. V.; Kraut-Vass, A.; Gaarenstroom, S. W.; Powell, C. J., NIST x-ray photoelectron spectroscopy database. https://srdata.nist.gov/xps. **2012**.

29. Aronniemi, M.; Sainio, J.; Lahtinen, J. Chemical state quantification of iron and chromium oxides using XPS: the effect of the background sustraction method. *Surf. Sci.* **2005,** 578, 108-123.

30. Irvine, J. T. S.; Sinclair, D. C.; West, A. R. Electroceramics: characterization by impedance spectroscopy. *Adv. Mater.* **1990,** 2, 132-138.

31. Hong, S.; Park, J.; Choy, J. Unusual maganetic property of Ba_2CrTaO_6 and phase transformation under high pressure. *J. Phys. Chem.* **1995,** 99, 6176-6181.

32. Goodenough, J. B.; Fafalas, J. Exploring the $A^{+}B^{5+}O_3$ compounds*. *J. Solid State Chem* **1973,** 6, 493-501.

33. Shpanchenko, R. V.; Nistor, L.; Van Tendeloo, G.; Van Landuyt, J.; Amelinckx, S.; Amelinckx, A. M.; Abakumov, E. V.; Kovba, L. M. Structural studies on new ternary oxides $Ba_8Ta_4Ti_3O_{24}$ and $Ba_{10}Ta_{7.04}Ti_{1.2}O_{30}$. *J. Solid State Chem.* **1994,** 114, 560-574.

34. Cao, W.; Yang, X.; Lu, F.; Zhu, W.; Liu, L.; Kuang, X.; Allix, M. 8H-10H stacking periodicity control in twinned hexagonal perovskite dielectrics. *Inorg. Chem.* **2018,** 57, 4117-4124.

35. Fang, L.; Li, C.; Peng, X.; Hu, C.; Wu, B.; Zhou, H. $Ba_4LiNb_{3-x}Ta_xO_{12}$ (x = 0-3): a series of high-Q microwave dielectrics from the twinned 8H hexagonal perovskites. *J. Am. Ceram. Soc.* **2010,** 93, 1229-1231.

36. Liu, L.; Flores, M.; Newman, N. Microwave loss in the high-performance dielectric $Ba(Zn_{1/3}Ta_{2/3})O_3$ at 4.2 K. *Phys. Rev. Lett.* **2012,** 109, 257601.

37. Tao, F.; Liang, C.; Wang, X.; Li, X.; Porcher, F.; Allix, M.; Lu, F.; Gong, H.; Liu, L.; Kuang, X. Shifted hexagonal perovskite $Ba_8MnNb_6O_{24}$: long-range ordering of high-spin d^5 Mn^{2+} layers and electronic structure. *Inorg. Chem.* **2018,** 57, 5732-5742.

38. Yu, X.; Chai, S.; Kuang, X.; Su, C.; Pan, F.; Fang, L.; Su, Q. Conductivity, dielectric loss, and electrical heterogeneous microstrcuture of eight-layer twinned hexagonal perovskite ceramics $Ba_8CuTa_6O_{24-\delta}$. *J. Am. Ceram. Soc.* **2013,** 96, 2510-2514.

For Table of Content Only

The covalent Cr-Cr and Cr-O-Cr bonding, the B-site vacancies and cationic ordering in the FSO sites relieving electrostatic repulsion stabilize the 8-layer twinned hexagonal perovskites $Ba_8Cr_{4-x}Ta_{4+0.6x}O_{24}$ with an extended range of B-site vacancy content and partial cation ordering among the FSO sites.

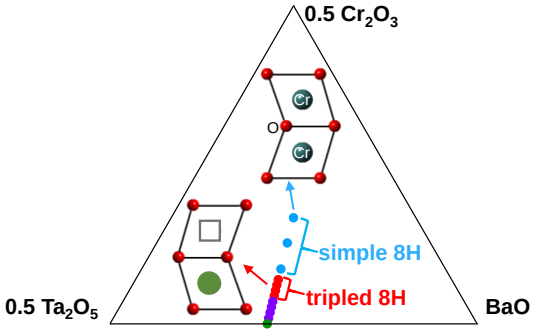

For Table of Content only